ACCSCIENCE PUBLISHING

Artificial Intelligence in Health

ORIGINAL RESEARCH ARTICLE

# Algorithm development and metal oxide nanoparticle analysis in magnetic resonance imaging: Advancing neurodegenerative disease diagnostics

**Daniela Gomes Bornal[1†], Hulder Henrique Zaparoli[1†], Marina Piacenti-Silva[2], Paulo Noronha Lisboa-Filho[2], and Marcela de Oliveira[2*]**

[1]Postgraduate Program in Science and Technology of Materials - POSMAT, School of Sciences/São Paulo State University, Bauru, São Paulo, Brazil

[2]Department of Physics and Meteorology, School of Sciences/São Paulo State University, Bauru, São Paulo, Brazil

(This article belongs to the *Special Issue: Artificial intelligence for diagnosing brain diseases*)

## Abstract

Magnetic resonance imaging (MRI) is critical in the diagnosis of neurodegenerative diseases, enabling the detection of brain lesions. Recent research has examined metallic nanoparticles (NPs) as MRI contrast agents (CAs) that can enhance lesion visibility by altering relaxation times. This study investigates the effects of metal oxide NPs on MRI relaxation times and brain lesion signals and proposes an algorithm for automated relaxation time determination using these NPs. The utilized NPs were synthesized using the sol–gel method and characterized using Fourier-transform infrared spectroscopy and X-ray diffraction. MRI scans were performed on a phantom infused with varying concentrations of each metal oxide NP to assess changes in pixel signal intensities and relaxation rates. Our analysis involved segmenting the MRI images to focus on regions with different NP concentrations. The algorithm computed the longitudinal relaxation time for each region, revealing that $Fe_2O_3$ NPs exhibited the most substantial effect on signal intensity and relaxation time. The results indicated a high correlation ($r = 0.9977$), demonstrating strong agreement and confirming the reliability of our method. Our findings suggest that metallic oxide NPs, particularly $Fe_2O_3$, can considerably alter magnetization and act as effective negative CAs in MRI. These capabilities can improve the monitoring and treatment efficacy of neurodegenerative diseases. Our method for quantifying longitudinal relaxation times can potentially enhance routine clinical MRI assessments, offering a promising tool for future clinical applications.

***Keywords:*** Magnetic resonance imaging; Algorithm; Longitudinal relaxation time (T1); Signal intensity

†*These authors contributed equally to this work.*

***Corresponding author:**
Marcela de Oliveira
(marcela.oliveira@unesp.br)

**Citation:** Bornal DG, Zaparoli HH, Piacenti-Silva M, Lisboa-Filho PN, de Oliveira M. Algorithm development and metal oxide nanoparticle analysis in magnetic resonance imaging: Advancing neurodegenerative disease diagnostics. *Artif Intell Health*. 2025;2(1):53-67. doi: 10.36922/aih.3947

**Received:** June 14, 2024

**Revised:** August 1, 2024

**Accepted:** August 28, 2024

**Published Online:** October 9, 2024

**Copyright:** © 2024 Author(s). This is an Open-Access article distributed under the terms of the Creative Commons Attribution License, permitting distribution, and reproduction in any medium, provided the original work is properly cited.

**Publisher's Note:** AccScience Publishing remains neutral with regard to jurisdictional claims in published maps and institutional affiliations.

## 1. Introduction

Magnetic resonance imaging (MRI) is a vital diagnostic imaging tool in the medical field, particularly for diagnosing various neurodegenerative diseases.[1,2] MRI can differentiate

between neurodegenerative conditions such as multiple sclerosis (MS), which is characterized by brain lesions primarily in the white matter. These lesions are identified through demyelination, inflammation, and axonal loss.[3,4] A comprehensive understanding of brain MRI findings is essential for accurate MS diagnosis.[5]

In MRI, a portion of proton nuclei within the body aligns parallel to an external magnetic field ($B_0$) to generate images.[6] These nuclei precess at a Larmor frequency ($w_0$) and are excited to an antiparallel state by a radio frequency (RF) pulse. On removing the RF pulse, the nuclei return to their equilibrium state, a process involving longitudinal (*T1*) and transverse (*T*2) relaxations.[6,7] *T*1 denotes the time required to reach 63% longitudinal magnetization, while *T*2 is defined as the time required for a decrease in the transverse magnetization by 37% its initial value.[8] Standard MRI sequences, including *T*1-weighted (*T*1-w), *T*2-weighted (*T*2-w), fluid-attenuated inversion recovery (FLAIR), and *T*1-weighted contrast modalities, are employed to detect overt lesions and assess tissue atrophy in MS.[2,9] MS lesions typically manifest as hyperintensities in *T*2-w and FLAIR images and as hypointensities in *T1*-w images.[2]

Recent research has revealed an imbalance in the metal levels among individuals suffering from MS, suggesting a link between metal levels and neurodegenerative diseases. This imbalance may contribute to brain injuries.[10-15] Metallic elements are considered potential causes of brain lesions. Furthermore, these metals are hypothesized to accumulate within lesions, altering the MRI contrast signal similar to contrast agents (CAs). However, the mechanism by which these metals influence the MRI signals of lesions remains underexplored.

Advancements in nanotechnology and the unique properties of metallic nanoparticles (NPs) that influence MRI relaxation times have facilitated the use of NPs as CAs in MRI.[1,8,16-19] Metallic NPs can reduce *T1* or *T2* by accelerating relaxation rates and inducing magnetic field inhomogeneity.[20] Regions containing these NPs appear bright in *T1*-w images, and NPs act as negative CAs, reducing *T2* signals.[16] CAs are essential for enhancing the contrast and sensitivity in MRI diagnostics. For instance, Gd is widely used as a CA in MRI, favored for its prolonged magnetic relation time and large magnetic moment.[21,22] Studies have also explored MRI CAs based on iron oxide ($Fe_2O_3$), gadolinium oxide, and manganese oxide NPs.[7,22-25] Cai *et al.* (2019)[21] highlighted advancements in the utilization of Mn oxide as a CA in MRI, while Blanco-Andujar *et al.*[24] emphasized the design of $Fe_2O_3$-based magnetic NPs that enable the optimization of their relaxivity for use as CAs in *T2*-w MRI.

The vast amount of data generated during MRI presents challenges for visual analysis, necessitating advanced analytical methods. Artificial intelligence-based algorithms are gaining prominence in the biomedical field and medical image analysis.[26] Automated image analysis enables the handling of extensive datasets with consistent precision, overcoming the limitations of manual methods. AI applications serve as decision support systems, although their development poses challenges.[27]

AI algorithms are widely used for targeting specific regions (organs or tissues), classifying disease stages, and diagnosing tumors.[28-31] For instance, Chang *et al.*[32] explored the use of a deep learning algorithm for the automated segmentation and quantification of the myocardial *T1* values, while Bidhult *et al.*[33] developed algorithms for *T1* and *T2* relaxation mapping in cardiac imaging. Specifically, for brain regions, Jibon *et al.*[34] improved a classification method to distinguish between cancerous and noncancerous tumors from brain MRI using log polar transformation and convolutional neural networks. In addition, the improved algorithm developed by Oliveira *et al.*[11] demonstrated the effectiveness of convolutional neural networks for detecting brain lesions in individuals with MS. In general, the primary role of AI is to create tools that automatically learn from data and produce accurate results,[35] potentially minimizing medical errors and aiding clinicians.[36]

Given the role of metal oxide NPs as CAs and importance of algorithms in medical image analysis, developing an algorithm to study NP signals in MRI is essential. This study investigates the relationship between different metal oxide NP concentrations and relaxation times, hypothesizing the following. (1) Various metal oxides affect signal intensity, (2) different metal oxide NP concentrations alter signal intensity, and (3) metal oxide NPs influence the longitudinal relaxation time in MRI. Moreover, we present an algorithm to analyze the signal intensity and autonomously determine relaxation times in MRI using metal oxide NPs.

## 2. Methods

### 2.1. Chemicals and reagents

Five distinct NPs were synthesized using the sol–gel method, a bottom-up chemical approach enabling enhanced control over procedural steps and the chemical compositions of the final products.[37] All reagents were sourced from Sigma-Aldrich, including cobalt(II) nitrate hexahydrate ($Co(NO_3)\cdot 6H_2O$, 98%), copper(II) nitrate tetrahydrate ($Cu(NO_3)_2\cdot 3H_2O$, 99%), iron(III) nitrate nonahydrate ($Fe(NO_3)_3.9H_2O$, 98%), nickel(II) nitrate hexahydrate ($Ni(NO_3)_2\cdot 6H_2O$, 97%), and

zinc oxide (ZnO, 99%). Additional reagents employed were ethylene glycol, citric acid, and nitric acid.

### 2.2. Synthesis of NPs

To synthesize $Co_3O_4$ NPs, $Co(NO_3)\cdot 6H_2O$ and urea were separately dissolved in 30 mL Milli-Q water at a molar ratio of 1:1, following which the solutions were combined and maintained at 30°C for 2 h for homogenization. The mixed solution was then heated to 80°C with vigorous stirring until complete solvent evaporation. $Co_3O_4$ NPs were finally obtained post-calcination at 400°C.[38]

Copper oxide (CuO) NPs, in the form of a $Cu_2O$/CuO nanocomposite, were prepared by dissolving 5 g $Cu(NO_3)_2\cdot 3H_2O$ in 20 mL ethylene glycol. After stirring the solution for 1 h, it was allowed to form a gel over 24 h, followed by drying at 200°C and calcination at 300°C for 1 h each. A final heat treatment was performed at 500°C for 1 h.

$Fe_2O_3$ NPs were synthesized by dissolving 7.2 g $Fe(NO_3)_3\cdot 9H_2O$ in 200 mL Milli-Q water and 32.6 g citric acid in 800 mL Milli-Q water. The iron nitrate solution was gradually added to the citric acid solution under constant stirring. The mixture was then heated to 90°C until gel formation, dried in an oven at 100°C for 24 h, and calcined at 400°C for 2 h. The resulting gel was ground into a powder.[39]

Nickel oxide (NiO) NPs were prepared by dissolving 3 g $Ni(NO_3)_2\cdot 6H_2O$ in 100 mL Milli-Q water. To this solution, 0.5 M sodium hydroxide solution was added drop-wise under continuous stirring until the pH reached 11, at which point precipitates were formed. These precipitates were washed 5 times with Milli-Q water, dried at 95°C to completely remove the solvent, and finally calcined at 550°C for 3 h.[40]

Zinc oxide (ZnO) NPs were synthesized using amorphous ZnO powder. Initially, 100 mL Milli-Q water and 15 mL nitric acid were mixed using a magnetic stirrer at 90°C, following which 5.5 g amorphous ZnO was added gradually. A secondary solution containing 190 mL deionized water and 5.5 g citric acid was prepared and mixed with the first solution. After 15 min of stirring and adding 10.5 mL ethylene glycol, the mixture was maintained at 290°C until reaching a basic pH. The temperature was then lowered to 180°C and subsequently to 70°C until the solvent was evaporated. Post-crystallization, the product was dried for 2 h at 350°C and further heated at 500°C for 30 min.[41]

### 2.3. Characterization of the NPs

#### *2.3.1. X-ray diffraction (XRD)*

XRD was used to determine the crystalline structures and phases of the NPs by comparing the results with the entries in the Joint Committee on Powder Diffraction Standards (JCPDS) database.[42] The crystallite sizes of the NPs were estimated using the Scherrer equation.[43] This size estimation was also conducted by analyzing XRD peaks, employing the Debye–Scherrer equation.[43] XRD spectra were acquired using a D/MAX-2100/PC (Rigaku) apparatus, equipped with a Cu Kα radiation source (λ = 1.5418 Å). The spectra were scanned in a 2θ range of 20 – 80°, with a scanning speed of 2°/min, a step size of 0.02°/min, and operating conditions of 40 kV and 20 mA.

#### *2.3.2. Fourier-transform infrared spectroscopy (FTIR)*

FTIR spectroscopy was performed to analyze the functional groups and molecular bonds within the NPs, facilitating the detection of compositional changes in the samples. This analysis was performed using a Vertex 70-Bruker spectrometer, supported by a diamond crystal. Spectra were acquired in the infrared region using the attenuated total reflectance method, with a scanning range of 3000 – 400 $cm^{-1}$, comprising 32 scans at a resolution of 4 $cm^{-1}$.

### 2.4. MRI

An acrylic phantom, simulating a brain, was filled with paramagnetic aqueous solutions to mimic different biological tissues, such as gray matter, white matter, and cerebrospinal fluid.[44] To assess changes in MRI signal intensity and relaxation time, four distinct concentrations of NPs (Table 1) were prepared and added to specific compartments of the phantom. The effects of these varying NP concentrations on MRI signal characteristics were subsequently evaluated.

The acquisition of MRIs followed a protocol recommended by the Consortium of MS Centers, tailored specifically for patients with MS. These images were acquired using a 3.0 Tesla Siemens Verio MRI scanner. To investigate the impact of varying NP concentrations on the MRI signals, signal quantification was performed across three different imaging sequences: *T1*-w, *T2*-w, and FLAIR. Furthermore, a study was performed to assess the influence of echo time (*TE*) variations on signal intensity, using TEs of 11, 32, 43, 64, and 86 ms. Figure 1 illustrates the phantom infused with different concentrations of the five metallic oxide NPs (Figure 1A) and a representative MRI slice of the phantom (Figure 1B).

**Table 1. Concentrations of nanoparticles (NPs) in the phantom**

| Hole | $Co_3O_4$ (g/L) | CuO (g/L) | $Fe_2O_3$ (g/L) | NiO (g/L) | ZnO (g/L) |
|---|---|---|---|---|---|
| 1 | 0.20 | 0.27 | 0.11 | 0.35 | 0.19 |
| 2 | 0.49 | 0.65 | 0.53 | 0.63 | 0.52 |
| 3 | 1.39 | 2.07 | 1.83 | 1.97 | 1.41 |
| 4 | 3.59 | 3.29 | 3.33 | 3.59 | 3.32 |

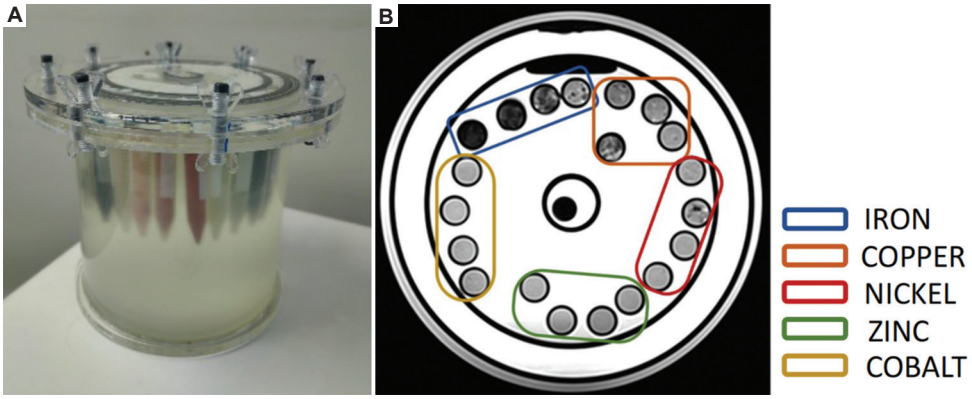


**Figure 1.** Phantom and its respective magnetic resonance imaging (MRI) for signal intensity analysis of the metal oxide nanoparticles (NPs). (A) Phantom used in the experiment. (B) MRI slice, with various metal oxide NPs being marked using different colors

### 2.5. Manual evaluation: MRI signal quantification and relaxation time evaluation

The MRI scans, obtained in the digital imaging and communications in medicine (DICOM) format, were manually analyzed using Image J and 3D Slicer software. A quantitative assessment of the mean signal intensity was performed for each compartment of the phantom, across various concentrations and *TE*. The manual calculation of *T1* relaxation time was executed using Equation I:

$$Y = A - Be^{\left(-\frac{TI}{T1}\right)} \quad \text{(I)}$$

where *Y* denotes the signal intensity, *TI* represents the inversion time, *A* signifies a scaling factor for each signal intensity, and *B* denotes the quality of inversion.[45] Furthermore, *T2* relaxation times were determined by fitting the *ET* signal curve using Equation II:

$$S(TE) = S_{máx}e^{\frac{TE}{T2}} + S_n, \quad \text{(II)}$$

where $S_n$ corresponds to the noise level in the image.[45]

### 2.6. Automatic evaluation: Algorithm development

The MRI images, obtained in the DICOM format, underwent preprocessing in three stages: (I) Reconfiguration to 1-mm$^3$ resolution, (II) application of an anisotropic diffusion filter, and (III) intensity correction for magnetic field inhomogeneity.[11] First, *T1*-weighted and *T2*-weighted images were resliced to an isotropic resolution of 1 mm$^3$ using cubic spline interpolation. Second, an anisotropic diffusion filter was employed to mitigate potential noise in the images.[46,47] Finally, image homogeneity was enhanced through bias correction using an N4ITK filter.[48]

After preprocessing, the algorithm segmented the region of interest (ROI) for the automatic determination of the longitudinal relaxation time (*T1*). Following this ROI segmentation, the algorithm autonomously calculated *T1* based on Equation I. For this, the algorithm detected and stored the signal intensity value *Y* by treating *A* and *B* as constants, and the *TI* value was input by the operator. Using these parameters, the algorithm automatically calculated and outputted the *T1* value. To validate and ensure the reproducibility of quantification, a Bland–Altman plot was created to compare automated *T1* quantification, with the manual approach using Equation I and Image J.[49,50]

## 3. Results

### 3.1. Characterization of the NPs

The chemical structures, crystal lattice indices, and crystallite sizes of the five NPs were determined using XRD and FTIR analyses. Figure 2 illustrates the combined chemical (FTIR) and structural (XRD) results of all NPs. The characteristic absorption bands of the metal–oxygen bond[51] were prominently observed at 1500 – 400 cm$^{-1}$. Furthermore, in all FTIR spectra, absorption bands were consistently observed at 2341 and 2358 cm$^{-1}$, likely attributable to atmospheric $CO_2$ absorption on metallic cations, a phenomenon that may have occurred within the apparatus during analysis.

The XRD spectrum of $Co_3O_4$ NPs in Figure 2A reveals distinct peaks at 2θ values of 31.45°, 37.17°, 38.79°, 45.10°, 59.72°, 65.54°, and 74.43°, corresponding to the lattice planes (220), (311), (222), (400), (511), (440), and (620), respectively. These peaks confirm the cubic phase of $Co_3O_4$ (JCPDS: 65-3103), with lattice parameters $a = b = c = 8.056$ Å.[38,52] The FTIR spectrum of these NPs in Figure 2B displays two vibrational modes at 667 and 561 cm$^{-1}$, indicative of Co–O bonds.[53,54]

Figure 2C presents the XRD spectrum of CuO NPs, where 2θ peaks aligned with the lattice planes (110), (111), (−112), (−202), (020), (202), (−113), (−311), (113), (311),

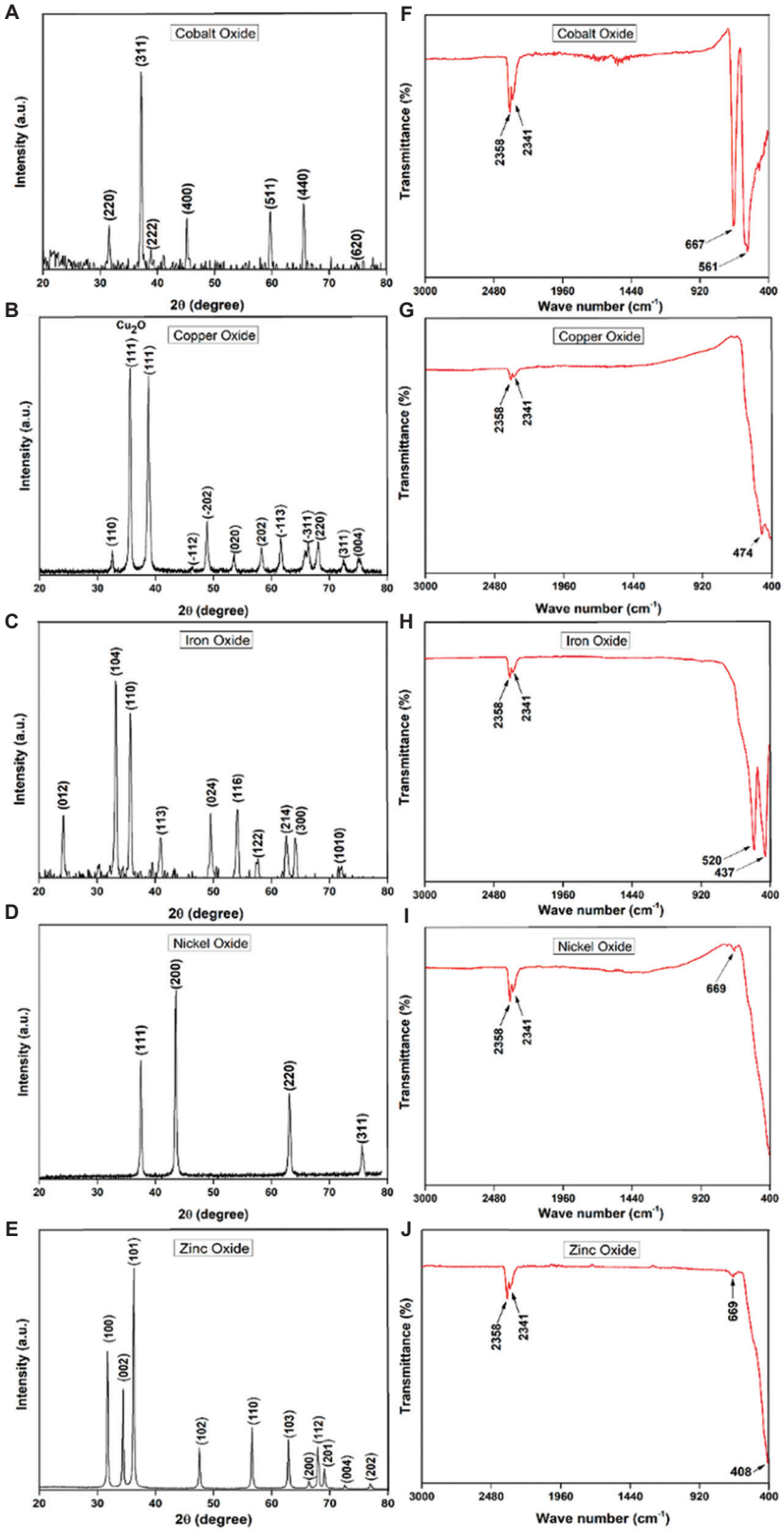


**Figure 2.** Characterization of nanoparticles by X-ray diffraction (XRD) and Fourier-transform infrared (FTIR). XRD patterns of (A) $Co_3O_4$, (C) CuO, (E) $Fe_2O_3$, (G) NiO, and (I) ZnO. FTIR spectra of (B) $Co_3O_4$, (F) $Fe_2O_3$, (H) NiO, and (J) ZnO

and (004). An additional peak at 35.58° corresponded to the (111) plane of the $Cu_2O$ phase. These peaks were consistent with the monoclinic phase of CuO (JCPDS: 89-5895), with lattice parameters $a$ = 4.682 Å, $b$ = 3.424 Å, and $c$ = 5.127 Å.[55] The FTIR spectrum of these NPs in Figure 2D presents a band at 474 $cm^{-1}$, denoting Cu–O formation.[56,57]

Figure 2E presents the XRD pattern of the $Fe_2O_3$ NPs, with peaks corresponding to rhombohedral $Fe_2O_3$ (JCPDS: 79-0007) and lattice parameters $a = b$ = 5.0285 Å and $c$ = 13.7360 Å.[39,58,59] The FTIR spectrum of these NPs in Figure 2F reveals absorption bands at 520 $cm^{-1}$ and 437 $cm^{-1}$, attributed to the Fe–O stretching and bending modes in hematite.[60]

In the XRD spectrum of NiO NPs displayed in Figure 2G, the peaks at 37.50°, 43.50°, 63.05°, and 75.58° corresponded to the lattice planes (111), (200), (220), and (311) of the cubic phase of NiO (JCPDS: 01-1239), with lattice parameters $a = b = c$ = 4.1710 Å.[40,61] The FTIR spectrum of these NPs in Figure 2H presents a prominent absorption band at 669 $cm^{-1}$, signifying Ni–O formation.[62]

In the XRD spectrum of ZnO NPs displayed in Figure 2I, the diffraction peaks aligned with the lattice planes (100), (002), (101), (102), (110), (103), (200), (112), (201), (004), and (202) of hexagonal ZnO (JCPDS: 65-3411), with lattice parameters $a = b$ = 3.249 Å and $c$ = 5.206 Å.[63,64] The FTIR spectrum of these NPs in Figure 2J illustrates a band at 408 $cm^{-1}$, corresponding to Zn–O bonding, and a band at 669 $cm^{-1}$, ascribed to C–H stretching in the alkyne group.[65,66]

The average crystallite size was estimated using the Debye–Scherrer equation

$$d = 0.89\lambda/\beta\cos\theta, \quad \text{(III)}$$

where 0.89 is the Debye constant, λ represents the X-ray wavelength (1.5406 Å), $\beta$ denotes the full-width at half-maximum of the peak, and $\theta$ represents the Bragg angle. The estimated average crystallite sizes for $Co_3O_4$, CuO, $Fe_2O_3$, NiO, and ZnO NPs were 12, 26, 21, 38, and 25 nm, respectively.

### 3.2. Manual evaluation: MRI signal and relaxation time evaluation

The acquired MRIs were manually evaluated to quantify the mean signal intensity in each compartment of the phantom across varying NP concentrations. Figure 3 illustrates the signal intensity as a function of the NP concentration for the *T1*, *T2*, and FLAIR sequences. Circles in Figure 3 represent the cross-sections of each compartment from which the mean pixel intensity was extracted. Notably, different NPs altered the MRI signal characteristics, with $Fe_2O_3$ NPs exerting particularly notable effects.

Figure 4 presents a series of curves demonstrating the relationship between signal intensity and NP concentrations, as well as the dependency of signal intensity on *TE* for these NPs in MRI. The results revealed that the pixel signal intensity is inversely proportional to the *ET* and NP concentration, a trend that was consistent across all the tested NPs. As the *ET* increased, a reduction in signal intensity was observed for all NPs. Furthermore, this reduction in signal intensity was more pronounced for NP concentrations with greater metal concentrations. Moreover, a steeper slope in the *T2* relaxation curve correlated with a greater decrease in the signal intensity, enhancing the effectiveness of the NPs as *T2* negative CAs.

In addition, Figure 4A-E illustrates variations in the signal intensities for the *T1*, *T2*, and FLAIR scan sequences as a function of the metal NP concentration. All metal oxide NPs exhibited a decrease in the signal intensity with increasing NP concentration across all three sequences consistently. Notably, $Fe_2O_3$ NPs exhibited a more pronounced signal reduction, while ZnO NPs demonstrated a slightly divergent behavior in the FLAIR sequence. Consequently, a steeper relaxation curve slope correlated with increased signal reduction, enhancing the efficacy of metal oxide NPs as CAs.

The magnitude of the *T2* contrast effect was quantitatively represented by spin–spin relaxivity $R_2$; an increase in the $R_2$ values indicated a corresponding increase in the contrast effect. The relaxation rate $R_2$ (=1/*T2*) is plotted against the *ET* in Figure 5A. An analysis of these curves revealed that NP concentrations directly impact the relaxivity time, thereby influencing the pixel intensity. In Figure 5B-D, which corresponds to the *T1*, *T2*, and FLAIR MRI sequences, respectively, the pixel intensity trends for each metal oxide NP were distinctly observed in relation to their concentrations. In particular, $Fe_2O_3$ NPs (depicted by the blue curve) demonstrated the most significant intensity variation across all sequences, showing a notable intensity decrease with increasing concentrations, which highlights their substantial impact on MRI imaging. Conversely, $Co_3O_4$ NPs (black curve) exhibited a more gradual decline, suggesting a less pronounced impact of their concentrations on MRI signal intensities. Other metal oxide NPs, including CuO (red curve), NiO (green curve), and ZnO (purple curve), also exhibited reductions in the pixel intensities with increasing concentrations; however, these changes vary, reflecting the distinct reactivity of each metal oxide NP in the MRI sequences. These differences underscore the importance of considering the unique properties of different metal oxide NPs when employing them as CAs in MRI to optimize image acquisition and interpretation.

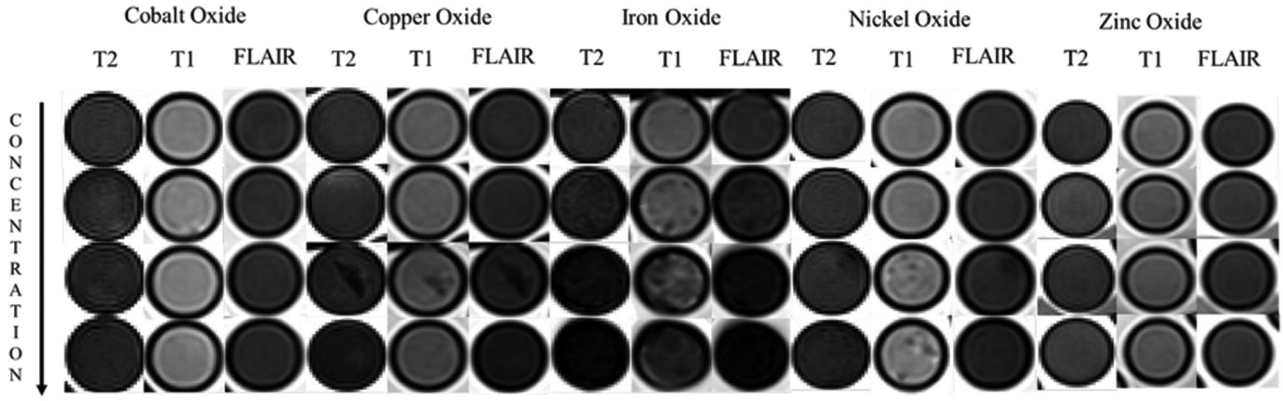


**Figure 3.** Magnetic resonance imaging: signal intensity as a function of nanoparticle concentration

### 3.3. MRI preprocessing, segmentation, quantification, and validation

Figure 6 offers a comprehensive and sequential overview of the entire MRI image analysis protocol. During the preprocessing stage, the images were subjected to three bias correction steps, uniformly applied to all slices within each specific examination sequence. An operator facilitated the selection of the particular slice for the ROI segmentation using a specialized algorithm designed to load all slices from the examination. Following this initial selection, meticulous segmentation of the ROIs was executed on the chosen slice. The subsequent stage involved quantifying the longitudinal relaxation time. This was accomplished by utilizing the signal intensity data extracted from the segmented ROIs in conjunction with Equation I. The final step of the algorithm computed and stored the average signal intensity for each of the segmented ROIs, thereby completing the intricate process of MRI image analysis.

To assess the reproducibility of our algorithm and validate it, a comparative analysis was conducted between the automatically computed *T1* values (derived from our algorithm) and manually determined *T1* values by experts. This comparison utilized the Bland–Altman plot (Figure 7A). The results revealed a close correspondence between the *T1* values obtained through the automated and manual methods, indicating a high degree of concordance. This was quantitatively supported by a correlation coefficient ($r$) of 0.9977, as illustrated in Figure 7B, thereby validating the accuracy and reliability of the algorithm in *T1* quantification.

## 4. Discussion

### 4.1. Signal intensities of the NPs and algorithmic analysis for MRI

Recent investigations into the signal intensities of NPs in MRI have highlighted notable advancements in the utilization of metal oxides, such as those of cobalt, copper, iron, nickel, and zinc, as CAs. Our findings indicated a decrease in pixel intensity across the *T1*, *T2*, and FLAIR sequences with increasing concentrations of these metal oxide NPs, suggesting enhanced proton relaxation. This effect was particularly prominent in the *T2* sequence, underscoring the potential of these NPs in influencing *T2* relaxation times and their effectiveness as CAs.

Further analysis of the effective *TE* graphs corroborated that all metallic oxide NPs under study resulted in decreased pixel intensity as *TE* increased. This characteristic aligns with the desirable attributes of CAs, highlighting the ability of these NPs to alter proton relaxation times in adjacent tissues. Notably, due to the different in local magnetic field disortions, each metal oxide NP exhibited different perturbations in the MRI signal, reflecting their different efficacies as CAs.

Our study demonstrated that different metallic oxide NPs interfere with the MRI signal intensity and variations in their concentrations alter the signal intensity and relaxation time, thus confirming our hypothesis. Specifically, varying concentrations of the $Fe_2O_3$ NPs displayed significant variations in both signal intensity and relaxation time, resulting in high contrast. This behavior was expected due to the magnetic properties of Fe. Furthermore, the $Fe_2O_3$ NPs exhibited CA characteristics in *T2*-w images, with higher concentrations resulting in lower signal intensities in *T1*-w sequences.

NPs synthesized in this study altered relaxation times in MRI, thereby modifying the pixel signal intensity. Our results revealed that these NPs displayed negative contrast, a characteristic influenced by the particle size. Specifically, NPs increased the signal intensity in *T1*-w images while decreasing the contrast intensity in *T2*-w images. This behavior is attributed to the fact that under a magnetic field, a magnetic dipole moment is induced

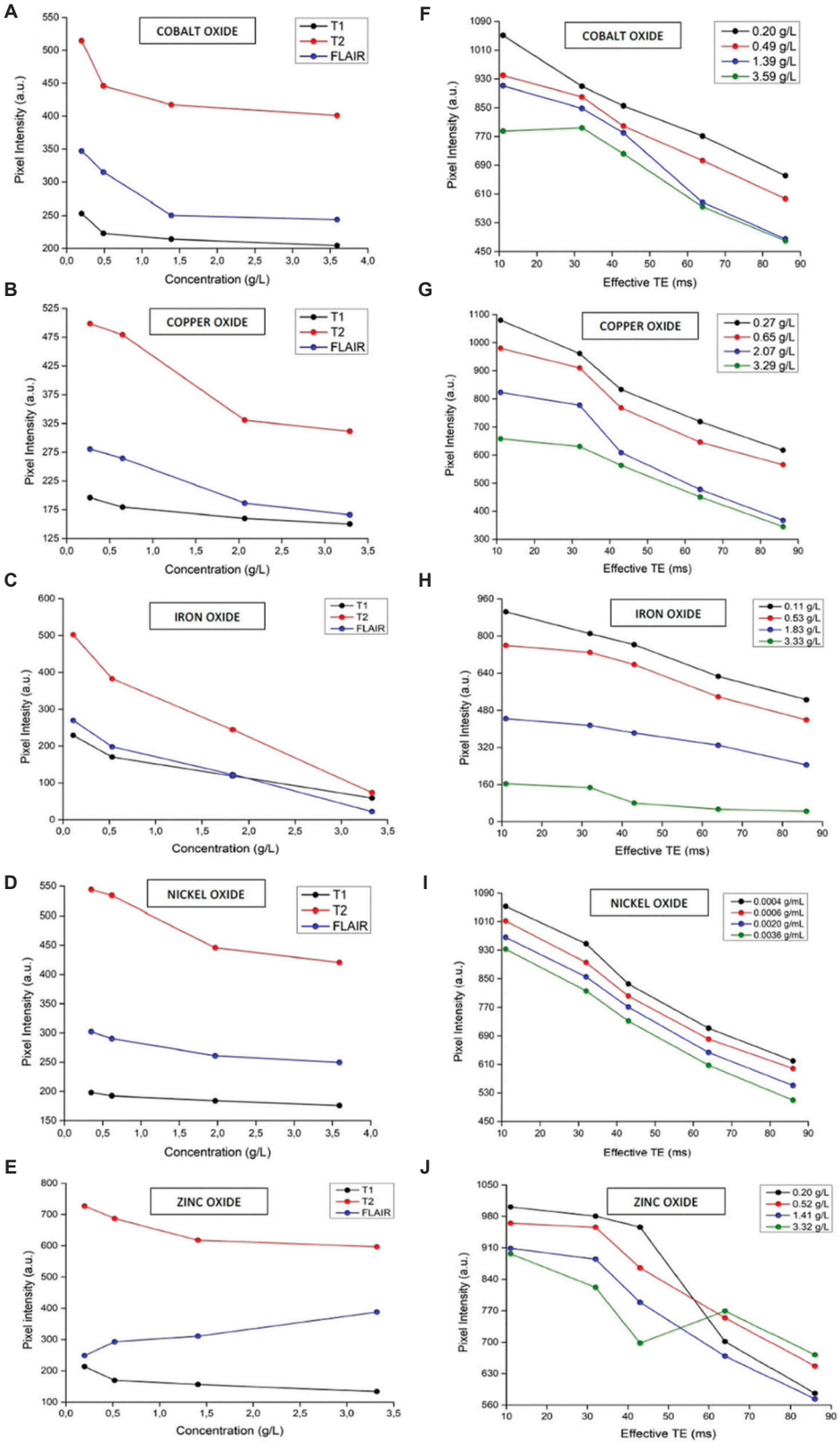


**Figure 4.** Signal intensity as a function of metal oxide nanoparticle concentration: (A) $Co_3O_4$, (C) CuO, (E) $Fe_2O_3$, (G) NiO, and (I) ZnO. Signal intensity as a function of *TE*: (B) $Co_3O_4$, (D) CuO, (F) $Fe_2O_3$, (H) NiO, and (J) ZnO

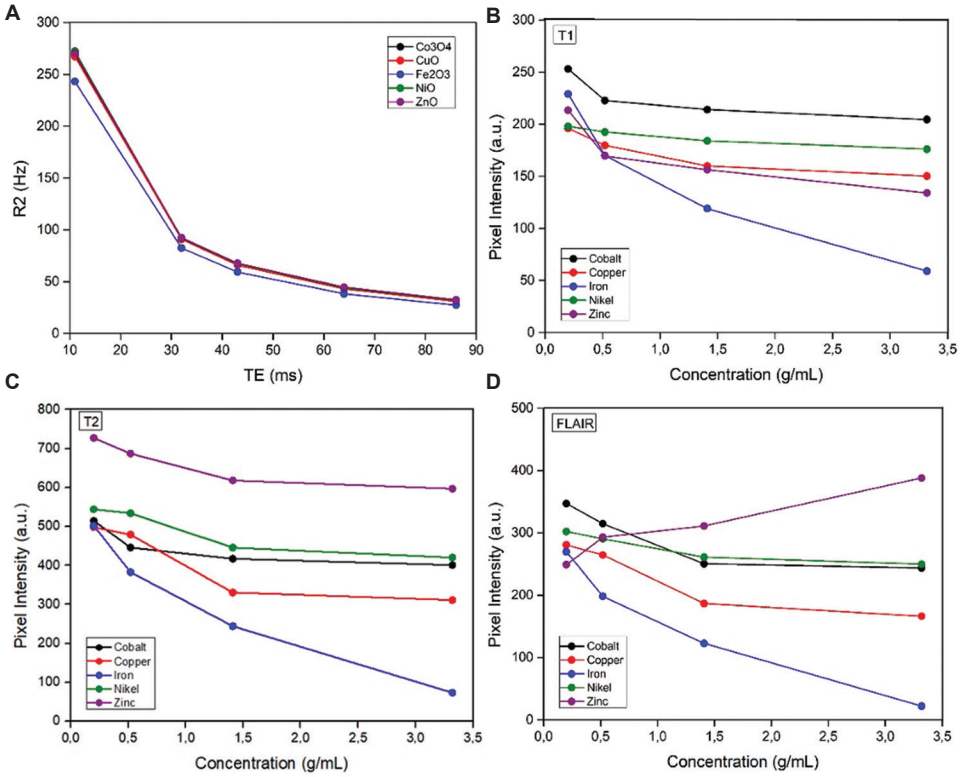


**Figure 5.** Comparison between different metal oxide nanoparticles for relaxation rate, T1, T2, and fluid-attenuated inversion recovery (FLAIR). (A) Relaxation rate $R_2$ as a function of echo time, (B) concentration as a function of *T1*, (C) concentration as a function of *T2*, and (D) concentration as a function of FLAIR for different NPs

in superparamagnetic NPs.[20] As water molecules diffuse toward the outer sphere of the induced dipole moment, the magnetic relaxation processes of water protons are disturbed, decreasing the spin-spin relaxation time (*T2*).[53] This disturbance causes darkening in the *T2*-w MRI images, corroborating our findings. In addition, Chen *et al.* (2022)[67] showed that the dimensions of nanomaterial's influence contrast, with NPs larger than 12 nm producing negative contrast. Our synthesized NPs, particularly $Fe_2O_3$ NPs, exhibited such a negative contrast characteristic, wherein higher concentrations resulted in darker areas. The signal reduction effect observed with increasing $Fe_2O_3$ NP concentration may be attributed to the disturbance of local magnetic field homogeneity caused by $Fe_2O_3$-core NPs.[68] This perturbation causes protons to lose energy owing to spin-spin interactions in an aqueous medium, increasing the loss of coherence and consequently decreasing the T2 time.[68]

As anticipated, $Fe_2O_3$ NPs substantially impacted the MRI signal intensity and longitudinal relaxation time. However, the other metal oxide NPs also demonstrated potential for specific applications based on their signal-altering properties in MRI.

Simultaneously, our algorithm for MRI analyses offers a transformative approach to MRI image interpretation. Traditional visual analysis by specialists often faces challenges with respect to subtle variations in the signal intensities associated with relaxation times. However, the implemented algorithm enables the automatic quantification of the longitudinal relaxation time, effectively overcoming these limitations. This tool segments different ROIs, analyzes signal intensity, and quantifies the longitudinal relaxation time for various NPs.

The reproducibility analysis of this method, validated against manual quantitative evaluations, revealed that the algorithm effectively assists specialists in identifying subtle variations in the signal intensity. This capability is particularly valuable when using different metal oxide NPs NPs as CAs. For example, $Fe_2O_3$ NPs exhibited substantial variations in the signal intensity and relaxation time, yielding high contrast, which aligned with the Fe magnetic properties. Moreover, the synthesized NPs altered the relaxation time in MRI, modifying the pixel signal intensity and displaying negative contrast influenced by the particle size.[67]

This algorithmic approach is particularly valuable in situations wherein changes in the signal intensity

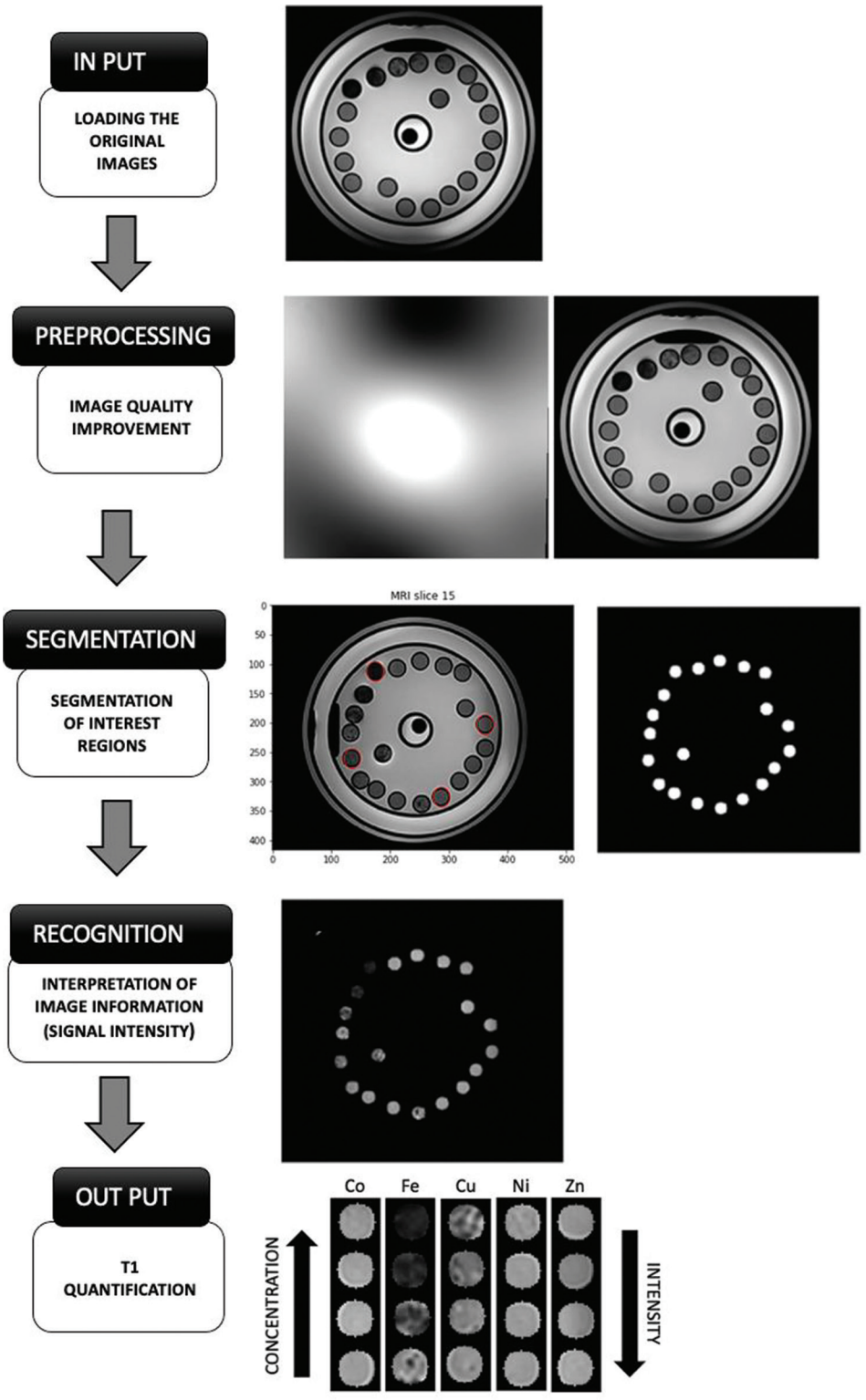


**Figure 6.** Flowchart of the proposed method. Input: Original magnetic resonance imaging. Processing: application of the bias correction filler. Segmentation: segmentation of all region of interests (ROIs). Recognition: signal intensity of all ROIs. Output: Quantification of the signal intensity for *T1* as a function of the metal oxide nanoparticle concentration

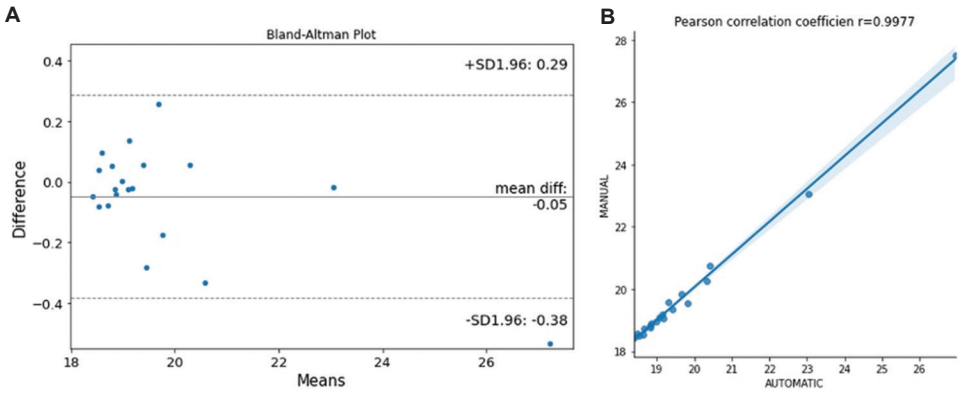


**Figure 7.** Validation. (A) Bland-Altman and (B) scatter plots comparing the *T1* values obtained from the automatic and manual quantification methods

are imperceptible to the naked eye. By automating the quantification process, this strategy enables a more precise and nuanced understanding of the impacts of different metal oxide NP concentrations on the signal intensity and relaxation time. The integration of our empirical data on the NP signal intensity, with the advancements facilitated by this algorithm, presents significant potential for MRI applications. This combined approach not only enhances the visual representation of anatomical structures and facilitates the detailed detection and characterization of diseases but also establishes a groundbreaking method for the quantitative assessment of signal intensity variations. Furthermore, this innovation represents a paradigm shift in imaging techniques, setting the stage for substantial advancements in the field of diagnostic medicine.

### 4.2. NPs as potential biomarkers

Studies on the effects of metal NPs on MRI signal intensities, particularly in the context of neurodegenerative processes, have garnered considerable attention. This is attributed to challenges encountered in identifying toxic metals that contribute to pathological changes in brains with neurodegenerative lesions. In addition, studies that have monitored cerebral lesions and analyzed metal elements involved in disease progression remain notably limited.

Existing studies indicate that metal elements can be detected in the brains of individuals with neurodegenerative lesions.[69-73] This suggests that the timing of image acquisition is crucial for patients as early active or acute lesions can influence the signal intensity. For instance, Tham *et al.* (2021)[69] displayed that early lesions contain substantially higher metal concentrations than acute lesions. If metal elements indeed impact the signal intensity in lesion regions, our study demonstrated that different metals can serve as biomarkers for monitoring brain lesions in patients with MS during disease progression.

Although the impact of NPs on the relaxation time may often be imperceptible in the visual analysis of the signal intensity due to subtle differences in contrast, the proposed automatic detection algorithm facilitates their use as biomarkers. Indeed, the reduction in the signal intensity with increasing NP concentration observed across the three image sequences (*T1*, *T*2, and FLAIR) in Figure 4 indicates that the largest differences occur at lower NP concentrations, where contrast changes are minimal. Hence, future research should focus on investigating NP signals at low concentrations and exploring the mechanism by which these metals relate to brain lesion progression in longitudinal studies.

### 4.3. Potential for clinical applications and diagnosis of neurodegenerative diseases

Our results offer new insights into the use of MRI for clinical applications, particularly for the detection and monitoring of brain lesions and neurodegenerative diseases. Notably, the contrast afforded by NPs, along with quantification achieved through our algorithm, enhances diagnostic capabilities. The ability to modulate contrast and signal intensities with different types of NPs can be beneficial across various medical diagnoses.

Despite these promising results, our study has some limitations. The nanometer scale of materials is highly sensitive, and the handling of nanomaterials requires meticulous attention, which complicates operations in low concentration ranges. Future research focusing on low concentration ranges may yield better correlations with neurodegenerative disease levels. In addition, given that the observed signals do not differentiate between the types of metals, signal specificity remains a limitation.

## 5. Conclusions

This study demonstrates that various concentrations of metallic NPs considerably influence MRI signal intensity,

impacting longitudinal relaxation time. In addition, we present an algorithm to analyze signal intensity and automatically determine relaxation times in MRI using metal oxide NPs. This innovative quantification holds considerable potential for enhancing treatment monitoring and routine clinical assessments in MRI analyses, particularly through the use of metallic oxide NPs as CAs. In contrast to the existing literature that predominantly focuses on a single type of NP, such as $Fe_2O_3$ NPs, our research encompasses a broader spectrum of metallic NPs, including $Co_3O_4$, CuO, $Fe_2O_3$, NiO, and ZnO NPs. This comprehensive exploration offers deeper insights into the versatile roles of different metallic NPs as CAs in MRI. Our study represents a substantial interdisciplinary achievement, integrating aspects of chemistry, physics, materials science, and medicine. It lays the groundwork for future innovations in MRI technology, particularly in tailoring CAs to meet the diverse requirements of clinical applications.

## Acknowledgments

None.

## Funding

This study was funded by the Brazilian agency Fundação de Amparo à Pesquisa do Estado de São Paulo (FAPESP 2020/03022-9, 2019/16362-5 and 2017/20032-5).

## Conflict of interest

The authors declare that they have no competing interests.

## Author contributions

*Conceptualization:* Marcela de Oliveira, Marina Piacenti-Silva
*Formal analysis:* Hulder Henrique Zaparoli, Marcela de Oliveira, Marina Piacenti-Silva
*Investigation:* All authors
*Methodology:* Daniela Gomes Bornal, Hulder Henrique Zaparoli
*Writing – original draft:* Daniela Gomes Bornal, Hulder Henrique Zaparoli, Marcela de Oliveira
*Writing – review & editing:* All authors

## Ethics approval and consent to participate

Not applicable.

## Consent for publication

Not applicable.

## Availability of data

The data utilized in this study are available from the corresponding author on reasonable request.

## References

1. Carr DH, Gadian DG. Contrast agents in magnetic resonance imaging. *Clin Radiol*. 1985;36(6):561-568.
doi: 10.1016/S0009-9260(85)80234-8
2. Bakshi R. Magnetic resonance imaging advances in multiple sclerosis. *J Neuroimaging*. 2005;15(4 Suppl):10-14.
doi: 10.1177/1051228405283362
3. Valverde S, Cabezas M, Roura E, *et al.* Improving automated multiple sclerosis lesion segmentation with a cascaded 3D convolutional neural network approach. *Neuroimage*. 2017;155:159-168.
doi: 10.1016/j.neuroimage.2017.04.034
4. Compston A, Coles A. Multiple sclerosis. *Lancet*. 2008;372(9648):1502-1517.
doi: 10.1016/S0140-6736(08)61620-7
5. Wang KY, Chetta J, Bains P, *et al.* Spectrum of MRI brain lesion patterns in neuromyelitis optica spectrum disorder: A pictorial review. *Br J Radiol*. 2018;91(1086):20170690.
doi: 10.1259/bjr.20170690
6. Zhang Y, Yang H, Zhou Z, Huang K, Yang S, Han G. Recent advances on magnetic relaxation switching assay-based nanosensors. *Bioconjug Chem*. 2017;28(4):869-879.
doi: 10.1021/acs.bioconjchem.7b00059
7. Na HB, Song IC, Hyeon T. Inorganic nanoparticles for MRI contrast agents. *Adv Mater*. 2009;21(21):2133-2148.
doi: 10.1002/adma.200802366
8. Lee N, Hyeon T. Designed synthesis of uniformly sized iron oxide nanoparticles for efficient magnetic resonance imaging contrast agents. *Chem Soc Rev*. 2012;41(7):2575-2589.
doi: 10.1039/C1CS15248C
9. Bakshi R, Thompson AJ, Rocca MA, *et al.* MRI in multiple sclerosis: Current status and future prospects. *Lancet Neurol*. 2008;7(7):615-625.
doi: 10.1016/S1474-4422(08)70137-6
10. de Oliveira M, Gianeti TMR, da Rocha FCG, Lisboa-Filho PN, Piacenti-Silva M. A preliminary study of the concentration of metallic elements in the blood of patients with multiple sclerosis as measured by ICP-MS. *Sci Rep*. 2020;10(1):13112.
doi: 10.1038/s41598-020-69979-9
11. de Oliveira M, Piacenti-Silva M, da Rocha FCG, Santos JM, Cardoso JS, Lisboa-Filho PN. Lesion volume quantification using two convolutional neural networks in MRIs of multiple sclerosis patients. *Diagnostics* (*Basel*). 2022;12(2):230.
doi: 10.3390/diagnostics12020230
12. Giacoppo S, Galuppo M, Calabrò RS, *et al.* Heavy metals

and neurodegenerative diseases: An observational study. *Biol Trace Elem Res*. 2014;161(2):151-160.

doi: 10.1007/s12011-014-0094-5

13. Forte G, Alimonti A, Pino A, *et al.* Metals and oxidative stress in patients with Parkinson's disease. *Ann Ist Super Sanita*. 2005;41(2):189-195.

14. Roos PM, Vesterberg O, Syversen T, Flaten TP, Nordberg M. Metal concentrations in cerebrospinal fluid and blood plasma from patients with amyotrophic lateral sclerosis. *Biol Trace Elem Res*. 2013;151(2):159-170.

doi: 10.1007/s12011-012-9547-x

15. Squadrone S, Brizio P, Abete MC, Brusco A. Trace elements profile in the blood of Huntington' disease patients. *J Trace Elem Med Biol*. 2020;57:18-20.

doi: 10.1016/j.jtemb.2019.09.006

16. Xiao YD, Paudel R, Liu J, Ma C, Zhang ZS, Zhou SK. MRI contrast agents: Classification and application (Review). *Int J Mol Med*. 2016;38(5):1319-1326.

doi: 10.3892/ijmm.2016.2744

17. Liu Z, Zhao M, Wang H, *et al.* High relaxivity Gd3+-based organic nanoparticles for efficient magnetic resonance angiography. *J Nanobiotechnology*. 2022;20(1):170.

doi: 10.1186/s12951-022-01363-3

18. Elhabiri M, Abada S, Sy M, *et al.* Importance of outer-sphere and aggregation phenomena in the relaxation properties of phosphonated gadolinium complexes with potential applications as MRI contrast agents. *Chemistry*. 2015;21(17):6535-6546.

doi: 10.1002/chem.201500155

19. Zheng R, Guo J, Cai X, *et al.* Manganese complexes and manganese-based metal-organic frameworks as contrast agents in MRI and chemotherapeutics agents: Applications and prospects. *Colloids Surfaces B Biointerfaces*. 2022;213:112432.

doi: 10.1016/j.colsurfb.2022.112432

20. Jun YW, Lee JH, Cheon J. Chemical design of nanoparticle probes for high-performance magnetic resonance imaging. *Angew Chem Int Ed Engl*. 2008;47(28):5122-5135.

doi: 10.1002/anie.200701674

21. Cai X, Zhu Q, Zeng Y, Zeng Q, Chen X, Zhan Y. Manganese oxide nanoparticles as MRI contrast agents in tumor multimodal imaging and therapy. *Int J Nanomedicine*. 2019;14:8321-8344.

doi: 10.2147/IJN.S218085

22. Olchowy C, Cebulski K, Łasecki M, *et al.* The presence of the gadolinium-based contrast agent depositions in the brain and symptoms of gadolinium neurotoxicity - A systematic review. *PLoS One*. 2017;12(2):e0171704.

doi: 10.1371/journal.pone.0171704

23. Wang J, Mei T, Liu Y, *et al.* Dual-targeted and MRI-guided photothermal therapy via iron-based nanoparticles-incorporated neutrophils. *Biomater Sci*. 2021;9(11):3968-3978.

doi: 10.1039/D1BM00127B

24. Blanco-Andujar C, Walter A, Cotin G, *et al.* Design of iron oxide-based nanoparticles for MRI and magnetic hyperthermia. *Nanomedicine*. 2016;11(14):1889-1910.

doi: 10.2217/nnm-2016-5001

25. Norouzi A, Rahim MSM, Altameem A, *et al.* Medical image segmentation methods, algorithms, and applications. *IETE Tech Rev*. 2014;31(3):199-213.

doi: 10.1080/02564602.2014.906861

26. Castiglioni I, Rundo L, Codari M, *et al.* AI applications to medical images: From machine learning to deep learning. *Phys Med*. 2021;83:9-24.

doi: 10.1016/j.ejmp.2021.02.006

27. Sharma N, Ray A, Shukla K, *et al.* Automated medical image segmentation techniques. *J Med Phys*. 2010;35(1):3-14.

doi: 10.4103/0971-6203.58777

28. Liu H, Ren L, Fan B, Wang W, Hu X, Zhang X. Artificial intelligence algorithm-based MRI in the diagnosis of complications after renal transplantation. *Contrast Media Mol Imaging*. 2022;2022:8930584.

doi: 10.1155/2022/8930584

29. Guo YY, Huang YH, Wang Y, Huang J, Lai QQ, Li YZ. Breast MRI tumor automatic segmentation and triple-negative breast cancer discrimination algorithm based on deep learning. *Comput Math Methods Med*. 2022;2022:2541358.

doi: 10.1155/2022/2541358

30. Liu B, Tan B, Huang L, *et al.* Intelligent algorithm-based picture archiving and communication system of mri images and radiology information system-based medical informatization. *Contrast Media Mol Imaging*. 2021;2021:4997329.

doi: 10.1155/2021/4997329

31. Wang X, Li X, Chen H, Peng Y, Li Y. Pulmonary MRI radiomics and machine learning: Effect of intralesional heterogeneity on classification of lesion. *Acad Radiol*. 2022;29:S73-S81.

doi: 10.1016/j.acra.2020.12.020

32. Chang S, Han K, Lee S, *et al.* Automated measurement of native T1 and extracellular volume fraction in cardiac magnetic resonance imaging using a commercially available deep learning algorithm. *Korean J Radiol*. 2022;23(12):1251-1259.

doi: 10.3348/kjr.2022.0496

33. Bidhult S, Kantasis G, Aletras AH, Arheden H, Heiberg E, Hedström E. Validation of T1 and T2 algorithms for quantitative MRI: Performance by a vendor-independent software. *BMC Med Imaging*. 2016;16(1):46.

doi: 10.1186/s12880-016-0148-6

34. Jibon FA, Khandaker MU, Miraz MH, *et al.* Cancerous and non-cancerous brain MRI classification method based on convolutional neural network and log-polar transformation. *Healthcare* (*Basel*). 2022;10(9):1801.

doi: 10.3390/healthcare10091801

35. Holzinger A, Plass M, Kickmeier-Rust M, *et al.* Interactive machine learning: Experimental evidence for the human in the algorithmic loop. *Appl Intell*. 2019;49(7):2401-2414.

doi: 10.1007/s10489-018-1361-5

36. Topol EJ. High-performance medicine: The convergence of human and artificial intelligence. *Nat Med*. 2019;25(1):44-56.

doi: 10.1038/s41591-018-0300-7

37. Modan EM, Plăiaşu AG. Advantages and disadvantages of chemical methods in the elaboration of nanomaterials. *Ann Dunarea Jos Univ Galati Fascicle IX Metall Mater Sci*. 2020;43(1):53-60.

doi: 10.35219/mms.2020.1.08

38. Priyadharsini CI, Marimuthu G, Pazhanivel T, *et al.* Sol-Gel synthesis of Co3O4 nanoparticles as an electrode material for supercapacitor applications. *J Sol Gel Sci Technol*. 2020;96(2):416-422.

doi: 10.1007/s10971-020-05393-x

39. Alagiri M, Hamid SBA. Sol-gel synthesis of α-Fe2O3 nanoparticles and its photocatalytic application. *J Sol Gel Sci Technol*. 2015;74(3):783-789.

doi: 10.1007/s10971-015-3663-y

40. Marlin V, Lugo C, Manuel P, *et al.* Synthesis and characterization of magnetic nickel used in dry rerforming of methane. *Revista Ciencia e Ingeniería.*. 2017;38:31-40.

41. Pires LA, de Azevedo Silva LJ, Ferrairo BM, *et al.* Effects of $ZnO/TiO_2$ nanoparticle and $TiO_2$ nanotube additions to dense polycrystalline hydroxyapatite bioceramic from bovine bones. *Dent Mater*. 2020;36(2):e38-e46.

doi: 10.1016/j.dental.2019.11.006

42. Gates-Rector S, Blanton T. The Powder Diffraction File: A quality materials characterization database. *Powder Diffr*. 2019;34(4):352-360.

doi: 10.1017/S0885715619000812

43. Ahammed KR, Ashaduzzaman M, Paul SC, *et al.* Microwave assisted synthesis of zinc oxide (ZnO) nanoparticles in a noble approach: Utilization for antibacterial and photocatalytic activity. *SN Appl Sci*. 2020;2(5):955.

doi: 10.1007/s42452-020-2762-8

44. Zaparoli HH, De Oliveira M, Lisboa-Filho PN, Piacenti-Silva M. Using zinc particles in a phantom to simulate multiple sclerosis lesions on magnetic resonance imaging. *Rev Bras Física Méd*. 2021;15:619.

doi: 10.29384/rbfm.2021.v15.19849001619

45. Oliveira E, Rocha M, Froner AP, Basso N, Zanini M, Papaléo R. Synthesis and nuclear magnetic relaxation properties of composite iron oxide nanoparticles. *Quim Nova*. 2018;42:57-64.

doi: 10.21577/0100-4042.20170309

46. Perona P, Malik J. Scale-space and edge detection using anisotropic diffusion. *IEEE Trans Pattern Anal Mach Intell*. 1990;12(7):629-639.

doi: 10.1109/34.56205

47. Gerig G, Kbler O, Kikinis R, Jolesz FA. Nonlinear anisotropic filtering of MRI data. *IEEE Trans Med Imaging*. 1992;11(2):221-232.

doi: 10.1109/42.141646

48. Tustison NJ, Avants BB, Cook PA, *et al.* N4ITK: Improved N3 bias correction. *IEEE Trans Med Imaging*. 2010;29(6):1310-1320.

doi: 10.1109/TMI.2010.2046908

49. García-Lorenzo D, Francis S, Narayanan S, Arnold DL, Collins DL. Review of automatic segmentation methods of multiple sclerosis white matter lesions on conventional magnetic resonance imaging. *Med Image Anal*. 2013;17(1):1-18.

doi: 10.1016/j.media.2012.09.004

50. Bland JM, Altman DG. Statistical methods for assessing agreement between two methods of clinical measurement. *Lancet*. 1986;1(8476):307-310.

51. Wu S, He M, Yang M, Zhang B, Wang F, Li Q. Near-infrared spectroscopy study of serpentine minerals and assignment of the OH group. *Crystals*. 2021;11(9):1130.

doi: 10.3390/cryst11091130

52. Packiaraj R, Devendran P, Venkatesh KS, Asath Bahadur S, Manikandan A, Nallamuthu N. Electrochemical investigations of magnetic Co3O4 nanoparticles as an active electrode for supercapacitor applications. *J Supercond Nov Magn*. 2019;32(8):2427-2436.

doi: 10.1007/s10948-018-4963-6

53. Binitha NN, Suraja PV, Yaakob Z, Resmi MR, Silija PP. Simple synthesis of Co3O4 nanoflakes using a low temperature sol-gel method suitable for photodegradation of dyes. *J Sol Gel Sci Technol*. 2010;53(2):466-469.

doi: 10.1007/s10971-009-2098-8

54. Farhadi S, Pourzare K, Sadeghinejad S. Simple preparation of ferromagnetic Co3O4 nanoparticles by thermal dissociation

of the [CoII(NH3)6](NO3)2 complex at low temperature. *J Nanostructure Chem*. 2013;3(1):16.

doi: 10.1186/2193-8865-3-16

55. Sundar S, Venkatachalam G, Kwon S. Biosynthesis of copper oxide (CuO) nanowires and their use for the electrochemical sensing of dopamine. *Nanomaterials*. 2018;8(10):823.

doi: 10.3390/nano8100823

56. Usha V, Kalyanaraman S, Thangavel R, Vettumperumal R. Effect of catalysts on the synthesis of CuO nanoparticles: Structural and optical properties by sol-gel method. *Superlattices Microstruct*. 2015;86:203-210.

doi: 10.1016/j.spmi.2015.07.053

57. Zayyoun N, Bahmad L, Laânab L, Jaber B. The effect of pH on the synthesis of stable Cu2O/CuO nanoparticles by sol-gel method in a glycolic medium. *Appl Phys A*. 2016;122(5):488.

doi: 10.1007/s00339-016-0024-9

58. Abdulkadir I, Abdallah HMI, Jonnalagadda SB, Martincigh BS. The effect of synthesis method on the structure, and magnetic and photocatalytic properties of hematite (α-Fe2O3) nanoparticles. *South Afr J Chem*. 2018;71:68-78.

59. Raja K, Mary Jaculine M, Jose M, *et al.* Sol-gel synthesis and characterization of α-Fe2O3 nanoparticles. *Superlattices Microstruct*. 2015;86:306-312.

doi: 10.1016/j.spmi.2015.07.044

60. Namduri H, Nasrazadani S. Quantitative analysis of iron oxides using Fourier transform infrared spectrophotometry. *Corros Sci*. 2008;50(9):2493-2497.

doi: 10.1016/j.corsci.2008.06.034

61. Shamim A, Ahmad Z, Mahmood S, Ali U, Mahmood T, Nizami ZA. Synthesis of nickel nanoparticles by sol-gel method and their characterization. *Open J Chem*. 2019;2(1):16-20.

doi: 10.30538/psrp-ojc2019.0009

62. Gogoi P, Saikia BJ, Dolui SK. Effects of nickel oxide (NiO) nanoparticles on the performance characteristics of the jatropha oil based alkyd and epoxy blends. *J Appl Polym Sci*. 2015;132(8):n/a-n/a.

doi: 10.1002/app.41490

63. Jung HJ, Lee S, Yu Y, Hong SM, Choi HC, Choi MY. Low-temperature hydrothermal growth of ZnO nanorods on sol-gel prepared ZnO seed layers: Optimal growth conditions. *Thin Solid Films*. 2012;524:144-150.

doi: 10.1016/j.tsf.2012.10.007

64. Patel M, Mishra S, Verma R, Shikha D. Synthesis of ZnO and CuO nanoparticles via sol gel method and its characterization by using XRD and FT-IR analysis. *Research Square. 2022*;1:1-13.

doi: 10.21203/rs.3.rs-1234162/v1

65. Kaningini AG, Azizi S, Sintwa N, *et al.* Effect of optimized precursor concentration, temperature, and doping on optical properties of ZnO nanoparticles synthesized via a green route using bush tea (*Athrixia phylicoides* DC.) leaf extracts. *ACS Omega*. 2022;7(36):31658-31666.

doi: 10.1021/acsomega.2c00530

66. Nayan MB, Jagadish K, Abhilash MR, Namratha K, Srikantaswamy S. Comparative study on the effects of surface area, conduction band and valence band positions on the photocatalytic activity of ZnO-MxOy heterostructures. *J Water Resour Prot*. 2019;11(3):357-370.

doi: 10.4236/jwarp.2019.113021

67. Chen C, Ge J, Gao Y, *et al.* Ultrasmall superparamagnetic iron oxide nanoparticles: A next generation contrast agent for magnetic resonance imaging. *Wiley Interdiscip Rev Nanomed Nanobiotechnol*. 2022;14(1):e1740.

doi: 10.1002/wnan.1740

68. Zottis ADA, Beltrame JM, Lara LRS, *et al.* Pheomelanin-coated iron oxide magnetic nanoparticles: A promising candidate for negative $T_2$ contrast enhancement in magnetic resonance imaging. *Chem Commun* (*Camb*). 2015;51(56):11194-11197.

doi: 10.1039/C5CC02536B

69. Tham M, Frischer JM, Weigand SD, *et al.* Iron heterogeneity in early active multiple sclerosis lesions. *Ann Neurol*. 2021;89(3):498-510.

doi: 10.1002/ana.25974

70. Butterworth RF. Metal toxicity, liver disease and neurodegeneration. *Neurotox Res*. 2010;18(1):100-105.

doi: 10.1007/s12640-010-9185-z

71. Kanda T, Nakai Y, Aoki S, *et al.* Contribution of metals to brain MR signal intensity: Review articles. *Jpn J Radiol*. 2016;34(4):258-266.

doi: 10.1007/s11604-016-0532-8

72. Chen P, Miah MR, Aschner M. Metals and neurodegeneration. *F1000Research*. 2016;5:366.

doi: 10.12688/f1000research.7431.1

73. Dales JP, Desplat-Jégo S. Metal imbalance in neurodegenerative diseases with a specific concern to the brain of multiple sclerosis patients. *Int J Mol Sci*. 2020;21(23):9105.

doi: 10.3390/ijms21239105